Effect of Steel Composition and Processing Parameters on the Penetration Depth of Microcracks in ZnFe-Coated Boron Steels

Henri Järvinen,* Jari Rämö, Ali Sabr, Sanna Järn, Emmi Lepikko, Martti Järvenpää, and Pasi Peura

Liquid metal assisted cracking (LMAC) and so-called microcracking are limiting the application of hot-dip galvanized boron steels in the direct press hardening process. This study addresses the role of steel hardenability on the microcracking behavior of ZnFe-coated (galvannealed) boron steels 22MnB5 and 22MnMoB8. Several soaking times and forming start temperatures in the range of 800–520 °C are examined using a laboratory press hardening equipment with a hat-profiled forming tool. The results indicate that the penetration depth of microcracks can be reduced by improving the hardenability of steel, which enables hot forming in austenitic state at exceptionally low temperatures even without accelerated cooling procedures. The austenite decomposition of 22MnB5 leads easily to heterogeneous microstructure (ferrite + austenite/martensite) below the coating/steel interface, which promotes the penetration of microcracks. The crack depth is generally reduced with a conversion-delayed 22MnMoB8 steel; however, a crucial reduction is attained only at lowest hot forming temperatures of 550 and 520 °C. The results of 22MnMoB8 uncouple the effect of high-temperature ferrite formation from the microcracking mechanisms and suggest that the embrittling effect from zinc or zinc-rich intermetallic phases plays a crucial role at conventional hot forming temperatures of 800–600 °C.

1. Introduction

In recent years, the automotive industry has faced an increasing demand for reducing CO_2 emissions without compromising

H. Järvinen, Dr. J. Rämö, A. Sabr, Prof. P. Peura
Engineering Materials Science
Tampere University
P.O. Box 589, FI-33014, Tampereen Yliopisto, Finland
E-mail: henri.jarvinen@tuni.fi

S. Järn, E. Lepikko, M. Järvenpää
SSAB Europe Oy
Harvialantie 420, FI-13300 Hämeenlinna, Finland

The ORCID identification number(s) for the author(s) of this article can be found under https://doi.org/10.1002/srin.202100112.

the safety performance of passenger cars.[1] These requirements have led to the increased use of ultrahigh strength boron steels, enabling reduced wall thicknesses of the car body components.[2] Currently, several car body components with an appealing combination of ultrahigh strength and complex geometries are manufactured using the direct press hardening process. In this process, the blank is first austenitized, subsequently hot formed at 800–650 °C, and simultaneously quenched in a die. The martensitic phase transformation of steel leads to ultrahigh strength and facilitates the attainment of excellent dimensional accuracy of the components.[3]

Use of coated steel sheets has constantly increased in the press hardening technology—a coating provides scaling protection during the austenitization treatment and improves corrosion resistance in service. Protective coatings can be economically applied as a part of steel strip production by means of continuous annealing and integrated hot-dipping processes. For several years, AlSi-coated 22MnB5 steel has dominated the market, but it is only able to provide barrier protection against corrosion.[4] Zinc-based coatings, Zn (also known as GI) and ZnFe (also known as GA or galvannealed), have higher potential against corrosion due to cathodic protection capability,[4,5] but are instead susceptible to the undesired cracking in hot deformation.[6] The cracking phenomena, as described earlier, for example, by Drillet et al.,[7] can be roughly divided into two groups: liquid metal assisted cracking (LMAC), or more generally known as liquid metal embrittlement (LME) and microcracking. Even though a number of ways have been developed to eliminate liquid phases and so LMAC, microcracks may occur at severe forming conditions.[7,8]

Regardless of the numerous studies, the root cause of microcracking has stayed partially unknown. Drillet et al.[7] emphasized the strong role of high friction forces in the origin of microcracking of zinc-coated 22MnB5. They also notified the simultaneously occurring ferrite formation below coating/steel interface and its possible correlation to the maximum crack depth. Kim et al.[9] investigated hot deformation of zinc-coated 22MnB5, ferritic–pearlitic 340Y steel, and fully austenitic

**ADVANCED
SCIENCE NEWS**

www.advancedsciencenews.com

**steel
research**
international

www.steel-research.de

twinning-induced plasticity (TWIP) steel and concluded that microcracks with equal penetration depth are formed regardless of the substrate microstructure. They also showed that increasing plastic strain (smaller die radius) increases the microcrack depth. Also, Köyer et al.[10] pointed out the strong role of plastic strain and suggested that the microcracks are formed in the regions which are first subjected to compressive stress and subsequently to tensile loading. In turn, Hensen et al.[8] proposed that the role of zinc, acting as an embrittling agent on steel grain boundaries, is essential contributor to microcracking. This finding is supported by the results of Janik et al.[11] who reported that longer annealing time and simultaneously reducing zinc content of the coating decreased the microcrack depth. Kang et al.[12] performed hot tensile tests after annealing at temperatures of 600, 700, 800, and 900 °C and concluded that the microcracking of zinc-coated 22MnB5 is facilitated by the presence of fine zinc-rich ferrite on the grain boundaries of the steel substrate. Based on the aforementioned literature, it can be outlined that the root cause of microcracking and resulting penetration depth must be a result of complex combination of mechanical, chemical, and tribological factors, which interplay during hot press forming (HPF) process. Still, uncoupling of the factors contributing to the microcracking of industrial HPF process has turned out to be challenging and requires further focus.

Even though the understanding on the microcrack formation has not been yet fully supplemented, there exists at least one commercial solution for limiting the microcrack depth below 10 μm, which is acceptance limit set by some car manufacturers.[13] Accordingly, Kurz et al.[14] reported that formation of deep microcracks is avoided when the hot forming of ZnFe-coated 22MnB5 steel is conducted at temperature range of 550–500 °C after an accelerated precooling step. To guarantee the robustness in industrial conditions, also the hardenability of the steel was later improved with higher Mn content of 2% to be used in the novel process technique.[15] Naturally, the LMAC is avoided at low hot deformation temperatures, but exact mechanisms leading to the significantly decreased penetration depth of microcracks with lower hot forming temperatures were not clarified. Also, Hensen et al.[16] applied accelerated cooling procedure for ZnFe-coated 22MnB5 steel, and performed HPF experiments at different hot forming temperatures. They estimated that reduced forming temperature below 600 °C may crucially prevent the embrittling effect of zinc by decreasing the mobility of zinc atoms to the austenite grain boundaries according to the proposed solid metal embrittlement (SME) mechanism. Therefore, hot forming at unconventionally low temperature may help to minimize both LME and SME, i.e, both proposed forms of metal-induced embrittlement (MIE) caused by zinc.

Even though role of zinc seems to be essential in the formation of deep microcracks, the researchers have faced difficulties in tracing the zinc at the prior austenite grain boundaries, which are known to provide favorable paths for propagating cracks.[17] In addition, the significance of subsurface ferrite formation has stayed unknown due to conflicting results between the studies conducted by Drillet et al.[7] and Kim et al.[9] In this study, we investigate the role of steel hardenability and hot forming temperature in two ZnFe-coated boron steels. The present study

focuses on the effect of forming start temperature which controls several secondary factors behind microcracking.

2. Experimental Section

2.1. As-Received Materials

The test materials consisted of two industrially produced hot-dip galvannealed, hereafter referred to as ZnFe-coated, steels with initial coating weight of 70 g m^{-2} per side. The sample materials were received as 1.5 mm-thick sheets in the coupon size of 110 × 100 mm. In addition to a standard 22MnB5 grade, a novel boron alloyed steel referred to as 22MnMoB8 was studied. The chemical compositions of the investigated steels are shown in **Table 1**.

Continuous cooling transformation (CCT) and time–temperature transformation (TTT) curves of the steels, calculated using thermodynamic simulation software JMatPro,[18] are shown in **Figure 1**. For comparison, the prior austenite grain size (PAGS) of 10 μm was used in the CCT calculations of both steels. Whereas there does not exist single universal method for measuring the grain size, the PAGS used in the calculations was roughly estimated based on the results presented in an earlier study.[19]

The CCT curves shown in Figure 1 indicate much greater hardenability of 22MnMoB8 due to higher amount of Mn and presence of Mo instead of Cr. In general, the critical cooling rate of 22MnB5 is typically reported to be around 30 °C s^{-1}.[20] The higher critical cooling rate of the present CCT diagrams (Figure 1a) is caused by the choice of smaller PAGS, which is an essential parameter in the calculation. In comparison, choosing the PAGS of 20 μm would result in the critical cooling rate of 20 °C s^{-1}.

2.2. Experimental Procedures

A laboratory custom-built press hardening equipment was used to investigate the material behavior in the direct press hardening process. HPF experiments were conducted using a water-cooled hat-profiled forming tool with a die geometry, as shown in **Figure 2**. Samples were austenitized in an electric chamber furnace at ambient atmosphere. An automatic sample transfer system was connected to a servohydraulic material testing machine MTS TestStar 810 with a load cell capacity of 100 kN. A pneumatically operated transfer system was used to move the samples from the furnace to the pressing tool, after which the pressing cycle was automatically started. The HPF was conducted without plate holding forces, i.e., the forming mode was the so-called crush forming instead of draw forming. These two forming methods have been discriminated and discussed, for example, in the study of Nakagawa et al.[21] As a

Table 1. Chemical compositions of the investigated steels.

Steel	C [%]	Si [%]	Mn [%]	Cr [%]	Mo [%]	Al [%]	Ti [%]	B [%]
22MnB5	0.23	0.26	1.26	0.21	0.05	0.031	0.042	0.0021
22MnMoB8	0.22	0.29	1.93	0.07	0.19	0.031	0.039	0.0027

**ADVANCED
SCIENCE NEWS**

www.advancedsciencenews.com

**steel
research**
international
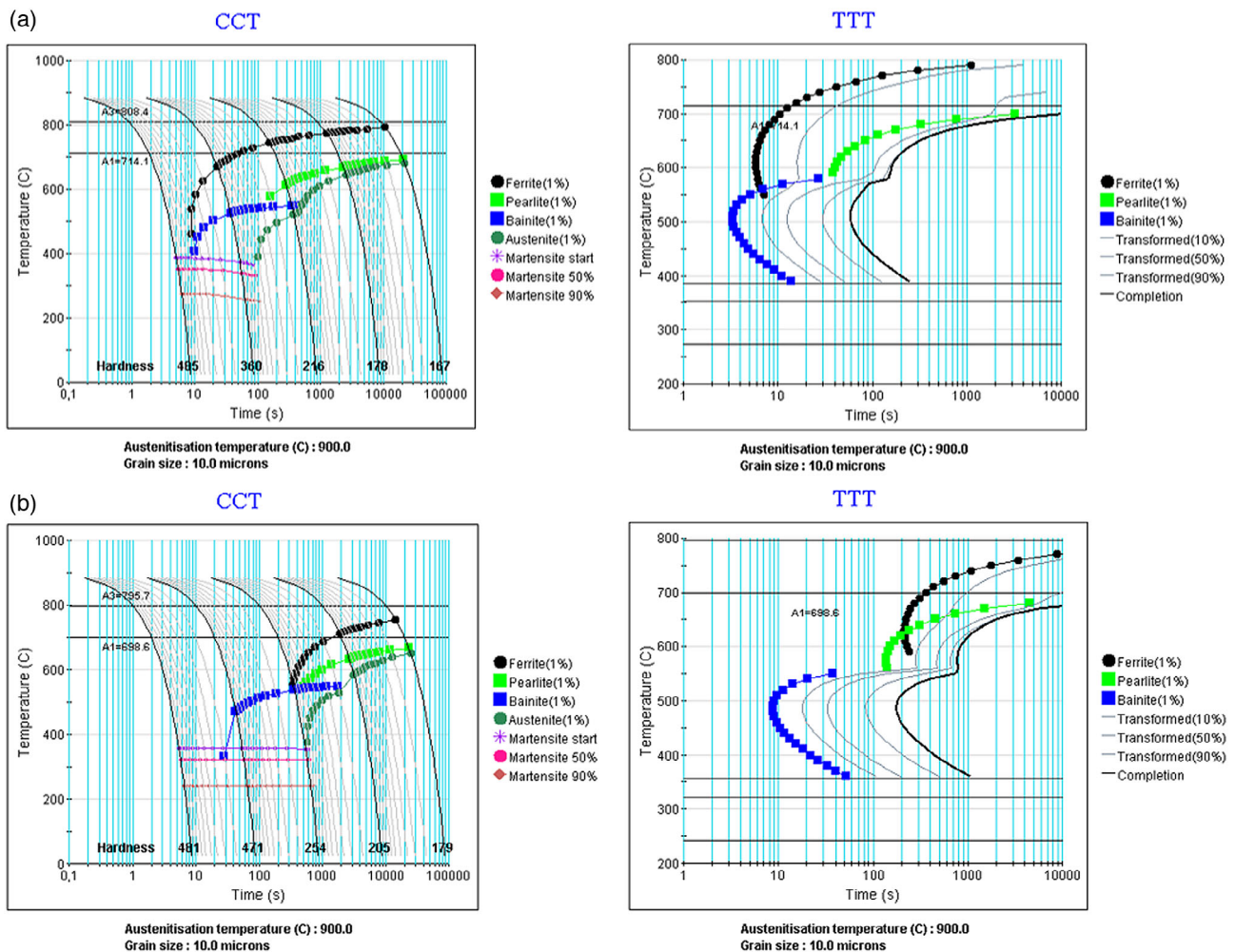
www.steel-research.de

Figure 1. CCT and TTT diagram of a) 22MnB5 and b) 22MnMoB8 calculated using JMatPro (version 10.2). In the graphs, the grain size of 10 μm refers to PAGS.

default, the tests were conducted without lubrication. However, two tests with selected parameters were performed in lubricated conditions. In those tests, the MoS_2 grease (MOLYKOTE) was used in the forming die.

Two types of HPF experiments were conducted in the current study: immediate hot press forming (IHPF) and delayed hot press forming (DHPF) experiments. In case of IHPF, the transfer time was ≈3 s resulting in the forming start temperature of around 850–800 °C. Due to fast cooling rate in the region of 900–800 °C, the forming temperature is more or less evaluated, hereafter referred only to as 800 °C. With this method, total annealing times of 180, 290, 450, 600, and 900 s in a furnace with a preset temperature of 900 °C were examined to attain different phase structures of the coating prior to hot deformation. The expressed times are total soaking times including both heating and annealing steps. The attained temperature after 180 s soaking was around 880 °C, whereas after longer soaking times the target temperature of 900 °C was reached. Specimen temperature was monitored throughout the process with spot-welded K-type thermocouples, which were connected to the materials testing machine through an external amplifier. The thermocouple was attached to region corresponding to the other end of the inner wall region of the

hat profile (Figure 2c). With this method, fully synchronized records of the press displacement (machine actuator), pressing force, and specimen temperature were obtained. **Figure 3**a shows an example of data recorded from HPF experiments.

In the DHPF experiments, the transfer step was intentionally delayed to decrease the start temperature of the forming by means of passive air cooling. The studied forming temperatures were 750, 700, 650, 600, 550, and 520 °C. It needs to be noted that these temperatures can be understood as targeted start temperatures of the hot forming step. In these experiments only two soaking times, 180 and 450 s, were examined using the following procedure. First, the complete temperature data of the passive air cooling were measured for both steels and soaking times from the middle point of the sheet to target the initial hot forming temperatures in the actual experiments (Figure 3b). After that, required air-cooling time to attain desired hot forming temperature for actual experiments was determined. However, it is worth noting that due to hardenability differences (Figure 1) the followed method resulted in variable microstructures at the time when the forming step was triggered.

In all experiments, the forming speed was set to a value of $40\,mm\,s^{-1}$. The maximum pressing force peak of 80–90 kN
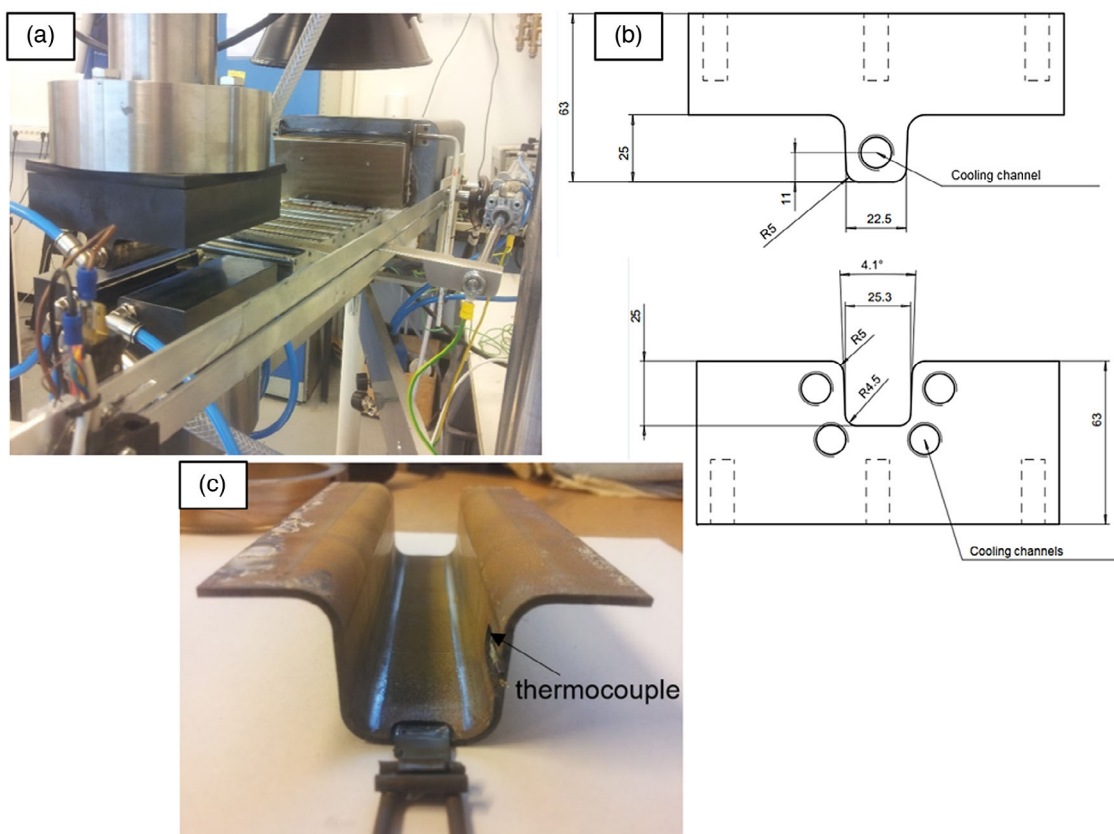
Figure 2. a) Experimental press hardening equipment. b) Die geometry of the hat-profiled forming tool used in the HPF experiments. c) Illustration of the location of thermocouple and method to attach sample to the automatic transfer system.
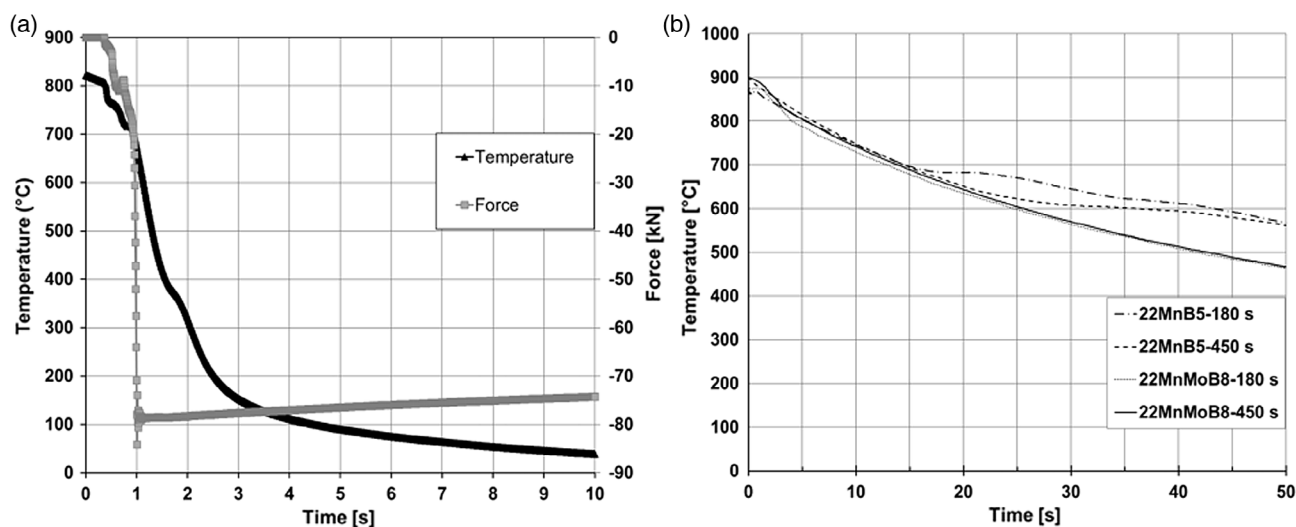

Figure 3. a) An example of data recorded from an IHPF experiment; b) air-cooling curves of the DHPF experiments.

was recorded as the bottom end was reached after 1 s movement of the piston. After that the pressing step was continued with target force of 70 kN for 30 s allowing the samples to cool down quickly below the room temperature. As shown in Figure 3a, temperature of around 50 °C was attained after the sample

had spent 10 s in a closed die. As a default, the HPF was conducted in as dry, i.e., without lubricant.

According to the data shown in Figure 3b, the passive air-cooling rate was 11–13 °C s^{-1} in the beginning of the air-cooling step, which corresponds to temperature range of 850–700 °C.

The cooling rate can be, however, slowed down due to latent heat release resulting from the austenite decomposition into ferrite, pearlite, or bainite (Figure 3b). This is seen as a clear drop in the slope of the air-cooling curves of 22MnB5. The longer austenitization time, 450 s, results in a delay of austenite decomposition. This behavior is connected to the larger grain size of austenite, which increases the hardenability of steel. In the case of 22MnMoB8 sharp slope change cannot be observed for either austenitization cycles. This indicates that no ferrite or bainite transformations occurred in 22MnMoB8 during passive air-cooling phase in the studied temperature range of 900–520 °C.

An infra-red (IR) thermal camera Telops FAST-IR 2K was used to evaluate the temperature uniformity of the sample during the passive air-cooling step. **Figure 4** shows IR camera images of a 22MnB8 sample air-cooled from 900 °C down to 520 °C.

Figure 4 shows that the front (right) and back (left) regions of the samples cooled down faster than the central regions. This natural effect was accelerated by the presence of support bars made of aluminum, which were in contact with the samples. Nevertheless, the central region of the samples, used in microstructural studies, shows only small temperature difference. The faster cooling of the front and back edge of the samples can,

however, affect the flow stresses formed in during HPF. In any case, it is evaluated that the used procedure allows reliable comparison between examined forming temperatures.

2.3. Microstructural Analysis and Characterization of the Cracks

All HPF samples were sectioned for microstructural analysis conducted with an optical microscope Nikon Eclipse MA 100. Supplementary evaluation was conducted using scanning electron microscope (SEM) Philips XL-30. The crack depth was measured from upper radius and outer wall regions of the hat-profiled samples (**Figure 5**). The measured crack depth is the distance between the coating/steel interface and crack tip. It is worth considering that some microcracks are halted to the coating/steel interface, and thus do not penetrate the steel. In case of the outer wall region, the percentage of the cracks penetrating the steel was also determined by dividing the penetrated cracks by the total number of cracks. Measuring of the depth of each penetrated crack allowed to analyze the crack profiles from the outer wall regions of the hat profiles (Figure 5b). In addition to crack analysis, the phase fractions of steel down to around 30 µm from
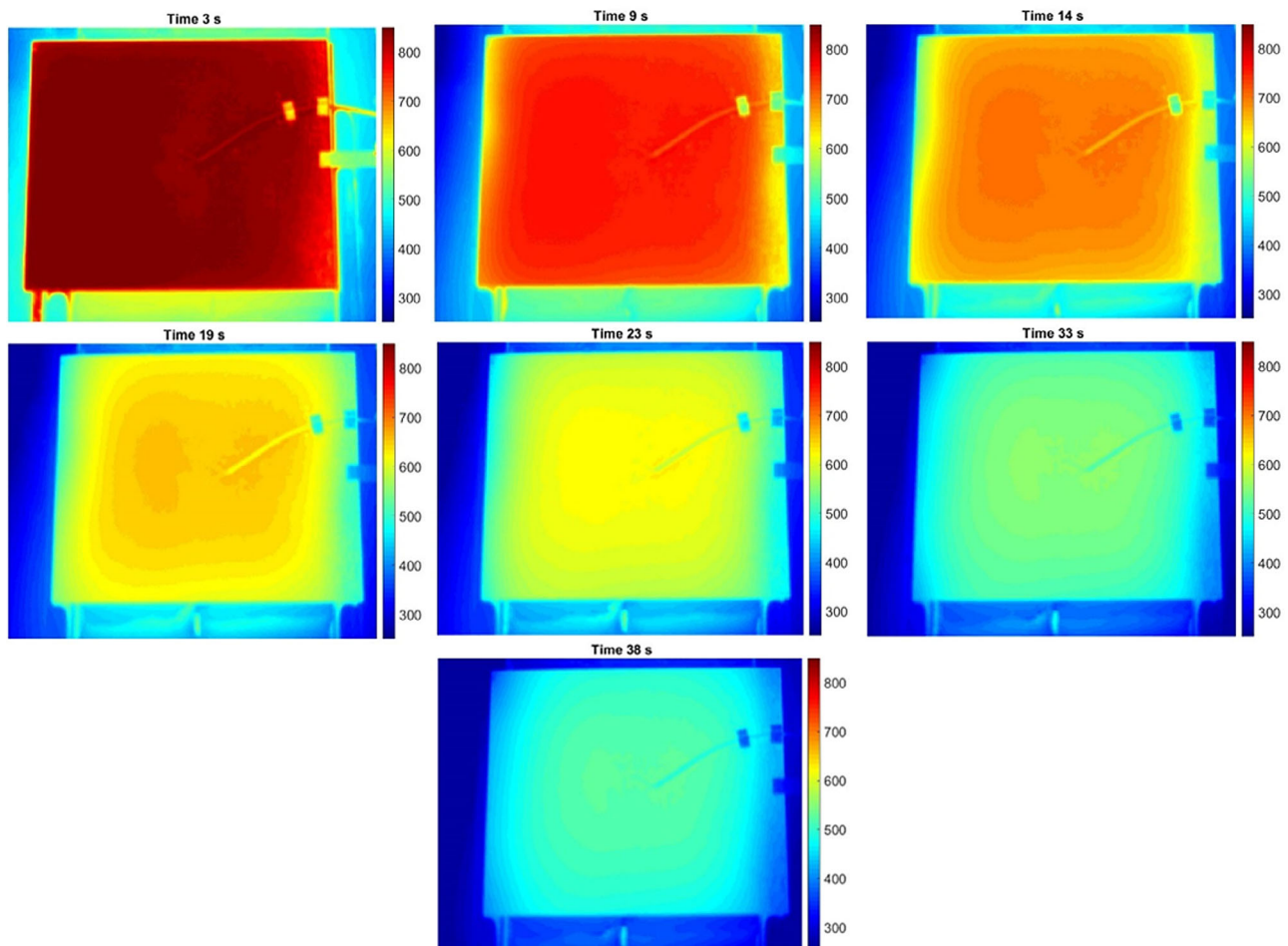

Figure 4. IR camera images of the DHPF samples of a 22MnMoB8 sample captured prior to hot forming target temperatures of 800 °C (3 s), 750 °C (9 s), 700 °C (14 s), 650 °C (19 s), 600 °C (23 s), 550 °C (33 s), and 520 °C (38 s). A thermocouple is attached in the central region of the sample.
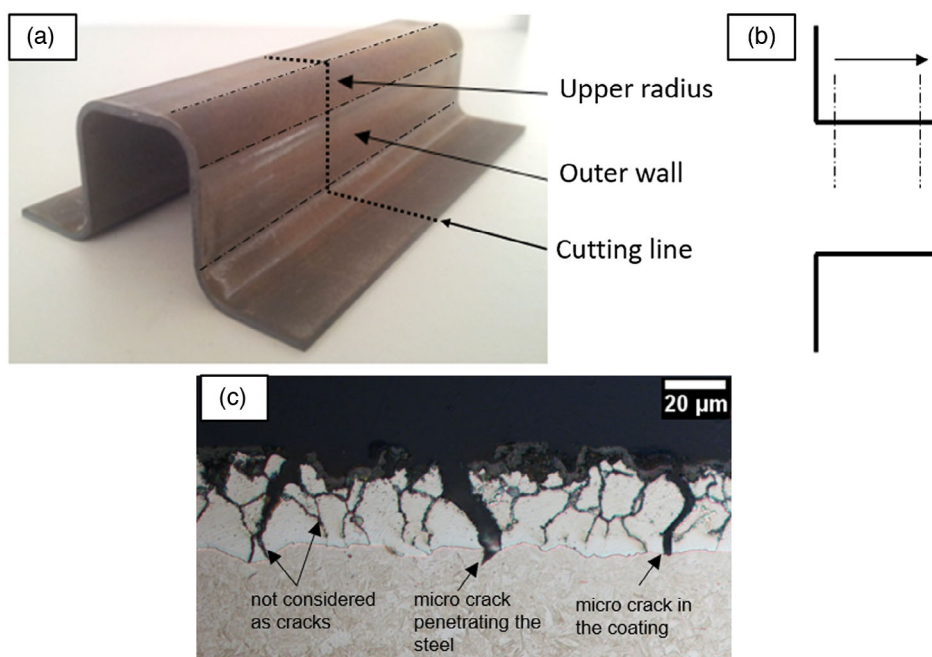
**ADVANCED
SCIENCE NEWS**

www.advancedsciencenews.com

**steel
research**
international

www.steel-research.de

Figure 5. a) Characterized areas of the hat-profiled hot press formed samples: upper outer radius and outer wall. b) A schematic drawing showing the direction of crack analysis conducted for the outer wall region. c) An optical micrograph observed from the outer wall region explaining the principles used in the crack analysis.

the coating/interface were evaluated from the optical micrographs. In this study, the expressed phase fractions are only used to see trends in the material behavior.

2.4. Elemental Analysis

A GDA750 glow discharge optical emission spectroscope Spectruma Analytik GmbH GDOES analysator was used to measure elemental depth profiles from surface across the steel/coating interface and down to a depth of at least 50 μm. Both as-received and HPF samples were used to analyze the changes in the chemical compositions occurring as a result of press hardening process. The measuring accuracy of the GDOES, generally described in ISO 16962:2005, can be divided into two parts: the accuracy of the depth axis (x-axis) is ±10% and the accuracy of the elemental mass fractions (y-axis) is considered as ±5% for the major elements with contents above 1 wt%. For the minor elements, the accuracy is lower and typically within ±5–20%

3. Results

3.1. As-Received Properties

The elemental depth profiles of as-received samples (**Figure 6**) reveal the differences in the C contents, i.e., the C content below coating/steel interface is higher for 22MnB5. The GDOES profile shown in Figure 6b suggests that the Mn content of as-received 22MnMoB8 is only 1.5–1.7% below coating/steel interface, which is lower than the nominal value of 1.93% (Table 1). In contrast, the Mo content is higher, i.e., 0.25–0.27% than the nominal

value of 0.19%. The initial coating thickness is around 8–10 μm. The small difference in the coating thicknesses between 22MnB5 and 22MnMoB8 can be explained with natural local variation. In 22MnMoB8 (Figure. 6b), the elevated Zn content far below the coating/steel interface can be considered as false signal, meaning that some Zn signal has been gathered from the edges of the formed crater after passing the interface.

3.2. Elemental Depth Profiles after Press Hardening

As indicated in the GDOES graphs of the HPF samples (**Figure 7**), the coating thickness increases constantly as a function of annealing time. In turn, the Zn content decreases with longer soaking time due to interdiffusion between Fe and Zn. It is worth considering that the B contents of HPF samples below coating/steel interface are much lower, i.e., only 5–15 ppm compared with the nominal values of around 30 ppm (Table 1). The depletion of B content must be caused by the enrichment of B in the upper regions of the coating, which results in decreasing B content below steel/coating interface as a function of annealing time. In case of 22MnMoB8 (Figure 7b,d,f), the aforementioned trends in Mn and Mo contents are the same for all annealing times of 180, 290, and 450 s.

To observe the possible effect of the passive air-cooling time on the development of the coating structure, the GDOES analysis was performed also to 22MnMoB8 samples formed at the lowest temperature of 520 °C. **Figure 8** shows the GDOES profiles of selected 22MnMoB8 samples formed at 520 °C.

The comparison between the GDOES profiles of IHPF (Figure 7b,f) and DHPF samples of 22MnMoB8 (Figure 8a,b)
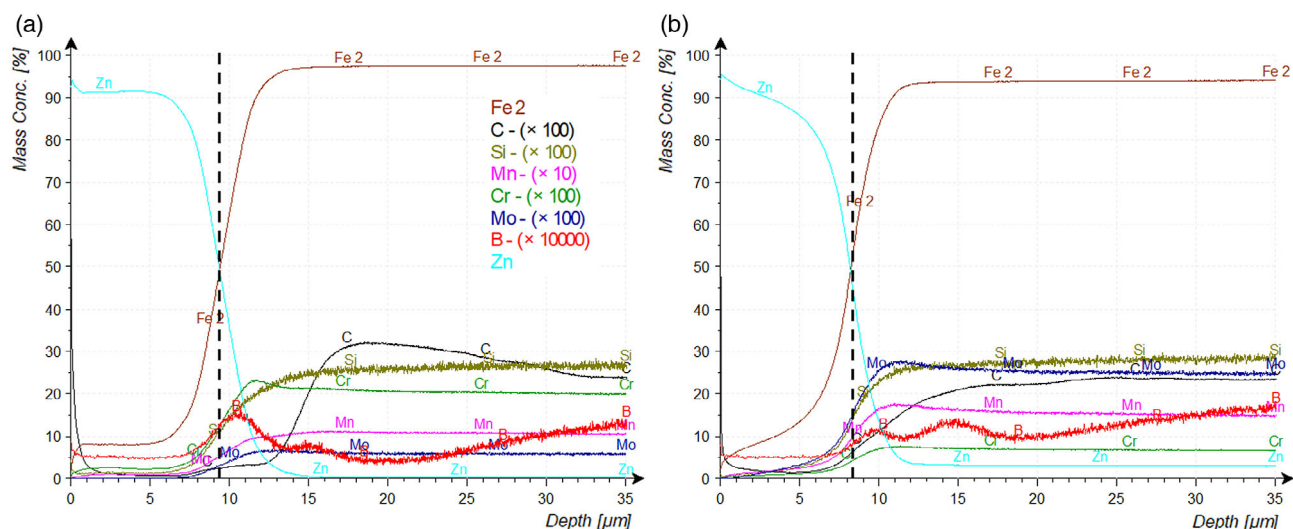
Figure 6. Elemental depth profiles of the as-received samples of a) 22MnB5 and b) 22MnMoB8. The dashed vertical line indicates the coating/steel interface. The curves of Al, Ti, and O are omitted for clarity. The legend presented in (a) is the same for both graphs.

does not reveal significant differences. The natural local variation in the coating thickness of the as-received samples can generally explain the small differences in the GDOES profiles of HPF samples.

3.3. Crack Characteristics and Microstructures

Table 2 shows the results attained in the crack and phase fraction analysis of IHPF samples. A dramatic drop in the crack depth can be observed at the long furnace times starting from 450 s. This trend is related to the elimination of liquid phases through the diffusion-controlled solidification of the coating layer. It can also be summarized that both average and maximum depth of the cracks are decreased with the prolonged annealing time in general. In case of 450, 600, and 900 s, the crack type can be seen purely as microcracks, whereas the liquid phases contribute to the penetration depth with the short soaking time of 180 s and more or less also in case of 290 s. The crack depth of 22MnMoB8 is relatively high with the annealing time of 290 s, indicating the incomplete elimination of liquid phases. The elemental profiles shown in Figure 7 support this finding by showing higher Zn content in 22MnMoB8 (Figure 7d) compared with 22MnB5 (Figure 7c). The difference can be observed, for example, by comparing the Zn contents at the depth of 10 μm.

Table 3 shows the results attained in the crack and phase fraction analysis of DHPF samples that is the test with varying forming start temperature. In case of 22MnB5, the low hot forming temperatures of 550 and 520 °C were not examined because the microstructure of the samples formed at 600 °C was already almost totally free of martensite, which is not desirable for the final properties and from the application point of view. The presented results (Table 3) show a generally decreasing trend in the crack depth of 22MnMoB8 as a function of decreasing forming start temperature. In turn, the behavior of 22MnB5 is not similar. 22MnB5 exhibited the formation of large amount of ferrite or ferrite (and pearlite) because of increasing passive air-cooling

time. In addition, the crack depth was decreased in the lubricated conditions. In particular, the number of cracks penetrating the steel was significantly reduced when using the lubricated die instead of nonlubricated die used as a default.

Representative optical micrographs and crack profiles of the outer wall region of the HPF samples of 22MnB5 and 22MnMoB8 (180 s/900 °C, forming start temperatures of 800, 700, and 600 °C) are shown in **Figure 9**. The optical micrographs show significant difference between 22MnB5 (left) and 22MnMoB8 (right): the amount of ferrite (and pearlite Figure 9e) is significantly higher in 22MnB5 and microcracks penetrating the steel are deeper. It is worth noting that the crack depth of 22MnMoB8 decreases as a function of forming start temperature and the subsurface microstructure of the steel stays essentially as martensitic. It can also be observed that oxidation of the grain boundaries of the α-Fe(Zn) grain of the coating is stronger after longer air-cooling time. Figure 9e shows exceptional appearance of the coating/steel interface and grain boundaries of α-Fe(Zn) in the coating. As a result of long passive air-cooling time (43 s), the microstructure of steel is almost completely ferritic–pearlitic. It is likely that similar phase transformations occur also at the interface where carbon is present.

Representative optical micrographs and crack profiles of the outer wall region of the DHPF samples of 22MnMoB8 (180 s/900 °C, forming start temperatures of 550 and 520 °C) are shown in **Figure 10**. The comparison between Figure 10a,b reveals a notable change in the appearance of the microcracks: the sample formed in the lubricated die does not reveal any microcracks with sharp crack tip. Small amount of fragmented ferrite or bainitic ferrite can be observed below coating/steel interface, even though the subsurface microstructure of the steel is still essentially martensitic after forming at exceptionally low temperatures of 550 and 520 °C.

Representative optical micrographs and crack profiles of the outer wall region of the HPF samples of 22MnB5 and 22MnMoB8 (450 s/900 °C, forming start temperatures of 800,
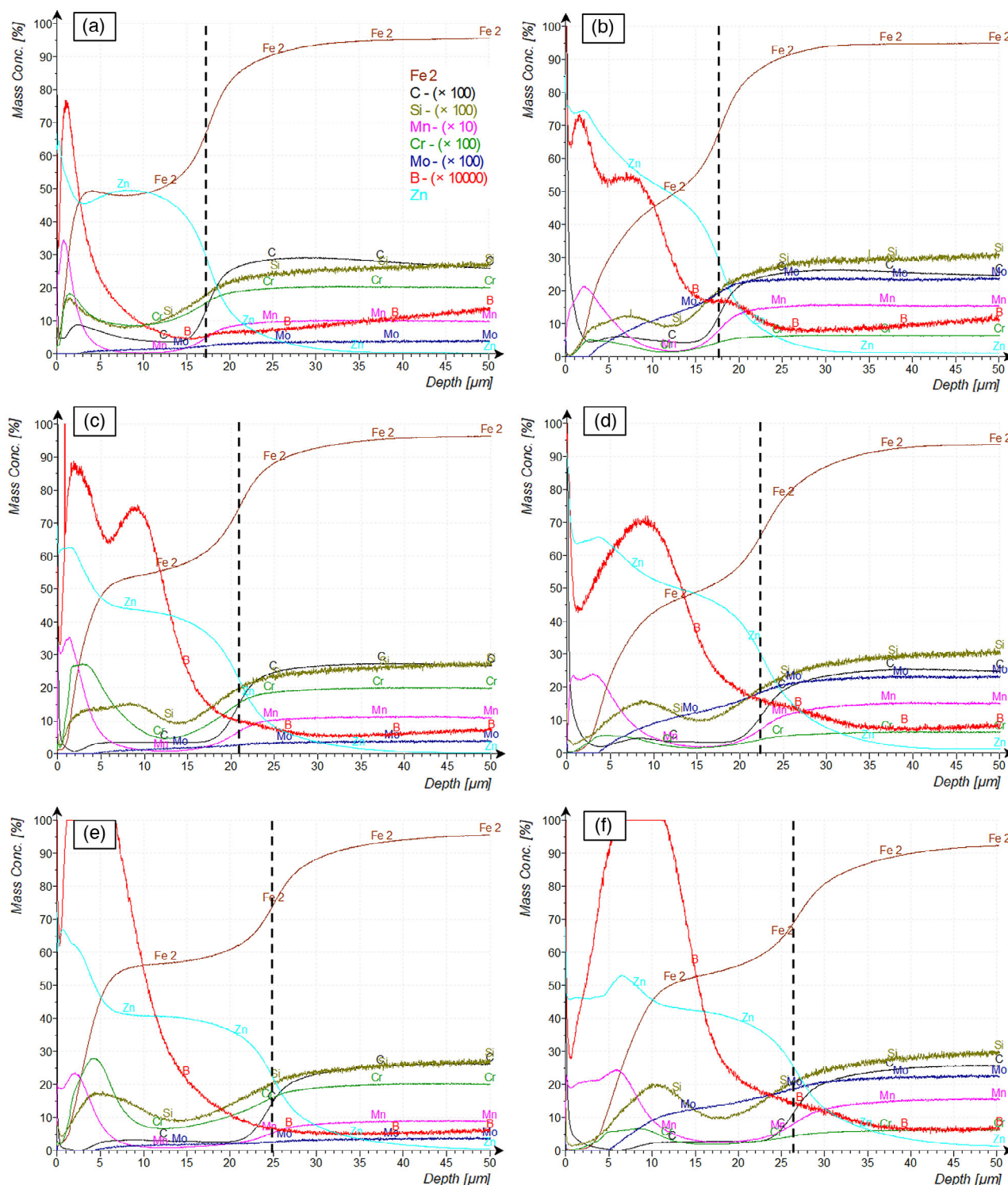
Figure 7. Elemental depth profiles of the IHPF samples of a) 22MnB5, 180 s/900 °C; b) 22MnMoB8, 180 s/900 °C; c) 22MnB5, 290 s/900 °C; d) 22MnMoB8, 290 s/900 °C; e) 22MnB5, 450 s/900 °C; and f) 22MnMoB8, 450 s/900 °C. The dashed vertical line indicates the coating/steel interface. The curves of Al, Ti, and O are omitted for clarity. The legend presented in (a) is the same for all graphs.

700, and 600 °C) are shown in **Figure 11**. Significant differences between studied steels of 22MnB5 (Figure 11a,c,e) and 22MnMoB8 (Figure 11b,d,f) can be again observed. Whereas

the microcrack depth of 22MnB5 increases with reducing forming temperature, the crack depth of 22MnMoB8 is almost constant for all forming temperatures of 800, 700, and 600 °C.
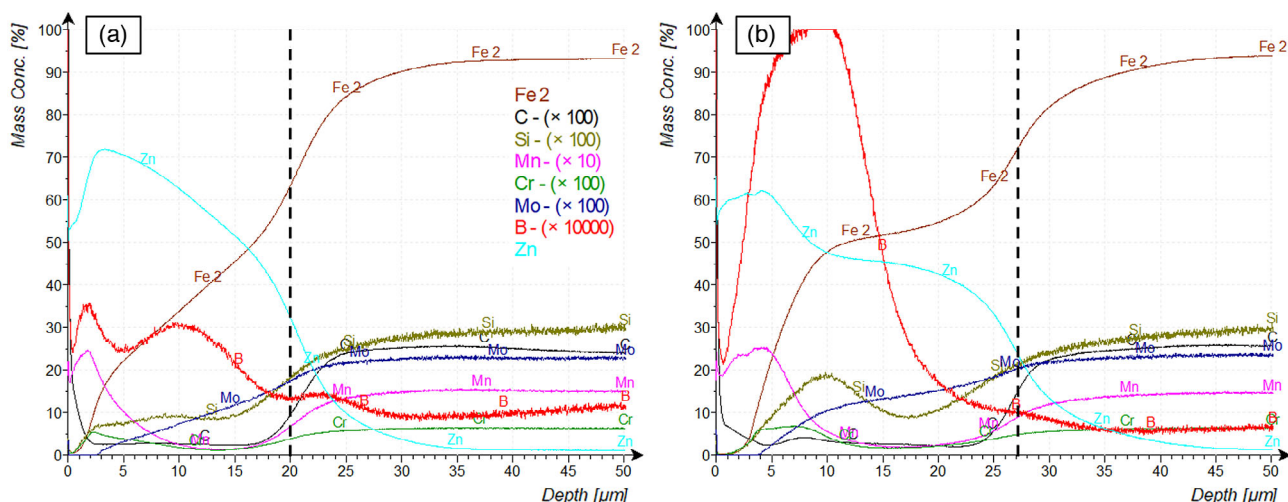
Figure 8. Elemental depth profiles of the DHPF samples of a) 22MnMoB8, 180 s/900 °C, forming start temperature of 520 °C; b) a) 22MnMoB8, 450 s/900 °C, forming start temperature of 520 °C. The dashed vertical line indicates the coating/steel interface. The curves of Al, Ti, and O are omitted for clarity. The legend presented in (a) is the same for both graphs.

Table 2. Summary of the crack and phase fraction analysis results of IHPF experiments, F = ferrite, M = martensite.

Steel	Furnace time [s]	Forming temperature [°C] and air-cooling time [s]	Crack depth max. [µm] upper radius	Crack depth max. [µm] outer wall	Crack depth avg. [µm] outer wall	Cracks in steel [%] outer wall	Phase fractions below coating down to 30 µm depth in steel [%]
22MnB5	180	800–3	169[a]	71[a]	18[a]	82	1 F–99 M
–	290	800–3	2	13	5	78	100 M
–	450	800–3	0	7	4	46	100 M
–	600	800–3	0	7	3	39	100 M
–	900	800–3	0	5	2	42	100 M
22MnMoB8	180	800–3	232[a]	63[a]	19[a]	54	100 M
–	290	800–3	70[a]	58[a]	19[a]	76	100 M
–	450	800–3	0	10	4	44	100 M
–	600	800–3			Not studied		
–	900	800–3			Not studied		

[a]LMAC identified.

Based on the observed images, the increasing crack depth of 22MnB5 seems to be connected with the microstructure of the steel: the amount of ferrite below coating/steel interface is strongly increasing as a function of passive air-cooling time. In turn, the microstructure of 22MnMoB8 is almost purely martensitic for all forming temperatures.

Representative optical micrographs and crack profiles of the outer wall region of the HPF samples of 22MnMoB8 (450 s/900 °C, forming start temperatures of 550 and 520 °C) are shown in **Figure 12**. The comparison between Figure 12a,b supports the observations mentioned earlier: lubricated conditions led to the absence of sharp V-shaped microcrack tips, indicating that the surface shear stresses are greatly diminished. Whereas the 22MnMoB8 samples formed in nonlubricated conditions at 550 and 520 °C show still the formation of shallow microcracks, the lubrication has eliminated the crack penetration into steel.

SEM imaging was used to observe the details of the subsurface microstructure with higher resolution; **Figure 13** shows an example of SEM micrographs of the HPF samples of 22MnB5. As seen in the SEM micrographs presented in Figure 13b,c, the formation of fragmented ferrite is stronger in vicinity of the cracks, which are acting as a strain concentration points during HPF. The image taken from the undeformed top area of the hat profile does not show ferritic phase constituents in steel.

4. Discussion

4.1. Role of Furnace Time/Annealing Time

Uncoupling of the LMAC and microcracking is required to outline the relationships between process parameters and penetration

Table 3. Summary of the crack and phase fraction analysis results of DHPF experiments, F = ferrite, M = martensite, p = pearlite.

180 [s]/900 °C

Steel	Forming temperature [°C] and air-cooling time [s]	Crack depth max. [μm] upper radius	Crack depth max. [μm] outer wall	Crack depth avg. [μm] outer wall	Cracks in steel [%], outer wall	Phase fractions below coating down to 30 μm depth in steel [%]
22MnB5	750–10	9	34	13	93	2 F–98 M
–	700–14	2	31	12	96	10 F–90 M
–	650–28	3	36	13	93	40 F–60 M
–	600–43	5	30	13	95	98 F + P–2 M
–	550			Not studied		
–	520			Not studied		
22MnMoB8	750–9	2	31	10	78	1 F–99 M
–	700–13	4	25	9	84	1 F–99 M
–	650–18	1	16	7	87	1 F–99 M
–	600–25	0	13	6	89	2 F–98 M
–	550–32	0	6	3	68	4 F–96 M
–	550–32[a)]	0	3	1	15	4 F–96 M
–	520–37	0	5	2	67	5 F–95 M

450 s/900 °C

Steel	Forming temperature [°C] and air-cooling time [s]	Crack depth max. [μm] upper radius	Crack depth max. [μm] outer wall	Crack depth avg. [μm] outer wall	Cracks in steel [%] outer wall	Phase fractions below coating down to 30 μm depth in steel [%]
22MnB5	800–3	0	7	4	46	1 F–99 M
–	750–10	0	12	6	83	2 F–98 M
–	700–14	0	19	8	82	10 F–90 M
–	650–20	0	26	12	85	15 F–85 M
–	600–30	0	25	12	88	95 F + P–5 M
–	550			Not studied		
–	520			Not studied		
22MnMoB8	800–3	0	10	4	44	100 M
–	750–10	4	23	7	82	2 F–98 M
–	700–14	0	13	5	74	1 F–99 M
–	650–19	0	19	6	77	1 F–99 M
–	600–26	0	13	5	72	1 F–99 M
–	550–33	0	8	4	70	2 F–98 M
–	550–33[a)]	0	0	0	0	2 F–98 M
–	520–38	0	5	2	77	4 F–96 M

[a)]Lubricated die.

depth of microcracks. For example, Janik et al.[22] identified that the presence of liquid zinc-rich phases can assist in microcrack penetration by embrittling the steel and result in deeper cracks also in the outer wall area of HPF samples. The mechanism of LMAC was explained by Cho et al.[23] They reported that diffusion of Zn to austenite grain boundaries promotes the immediate formation of zinc-rich ferritic film, α-Fe(Zn), on austenite grain boundaries, facilitating the typically observed macroscopic cracking. In the current study, the upper radius of the hat profiles was first analyzed to identify the contribution of LMAC mechanism which typically manifests itself in the form of severe deep cracks

in the outer radius of the profiles. The tests where liquid phases were clearly involved have been identified (marked in Table 2) and will be ruled out of the scope of further discussions focusing mainly on the microcracking itself.

The elimination of liquid phases cannot be guaranteed with any combinations of high hot forming temperatures (above 750 °C) and short annealing times of 180–290 s. In turn, the longer annealing times of 450, 600, and 900 s should result in quasi-complete or complete solidification of the coating layer. In fact, the elimination of liquid phases can only be justified by means of X-ray diffraction and absence of intermetallic Γ-phase (Fe_3Zn_{10}), which is the
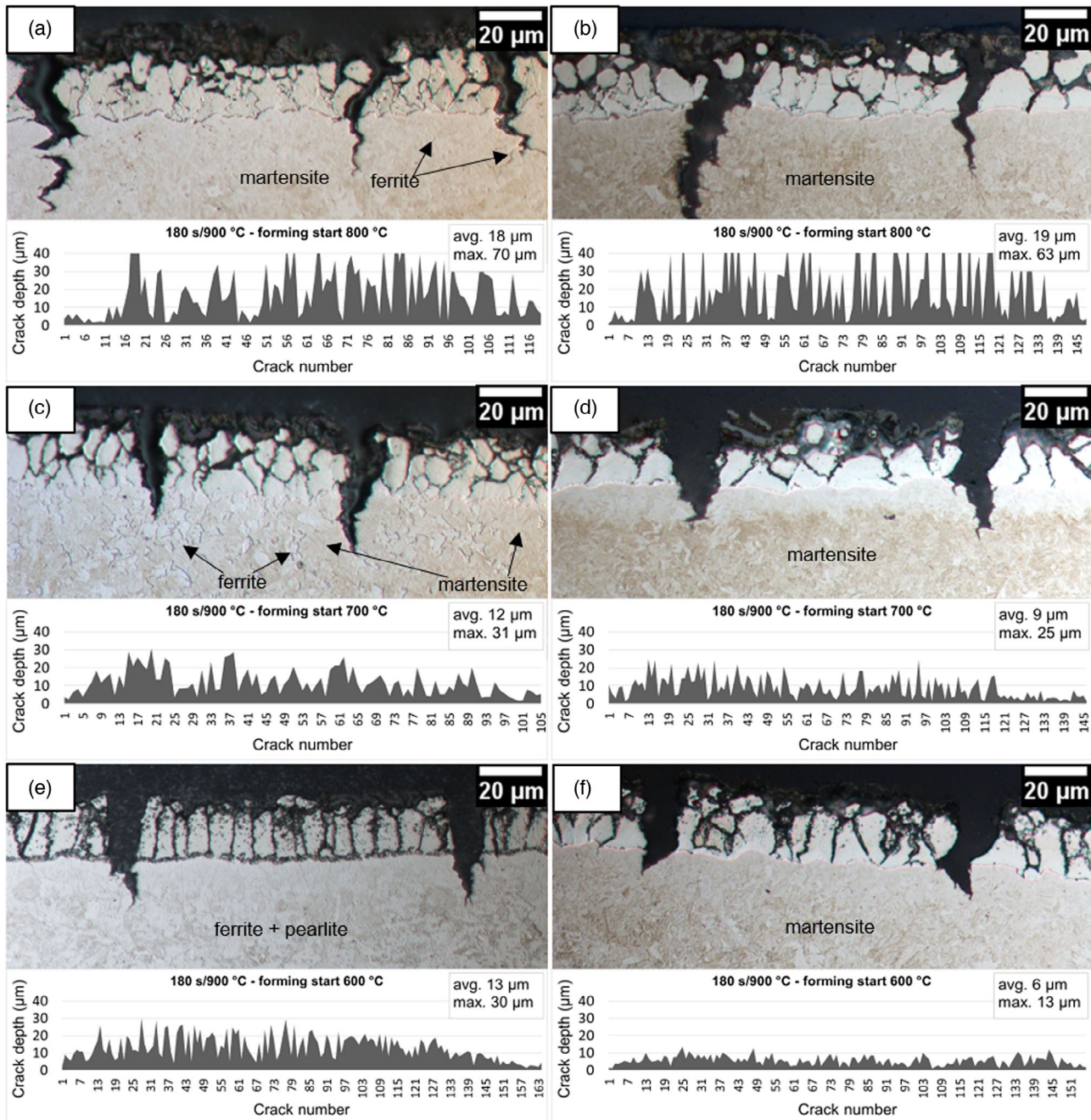
Figure 9. Optical micrographs and crack profiles of the outer wall regions of the HPF samples annealed for 180 s at 900 °C. a) 22MnB5–800 °C; b) 22MnMoB8–800 °C; c) 22MnB5–700 °C; d) 22MnMoB8–700 °C; e) 22MnB5–600 °C; and f) 22MnMoB8–600 °C. Etching with 2% Nital.

solidified product from zinc-rich liquid.[24] The gradual decrease in T-phase by annealing time and temperature was discussed in the earlier study.[25] Similar results have been reported elsewhere.[24] As also confirmed by the elemental profiles (Figure 7), the longer furnace times resulted in the decreased Zn content of the coating. Considering the results of IHPF experiments (Table 2), the prolonged annealing time decreased the penetration depth of microcracks. More interestingly, the combination of the highest forming temperature of 800 °C and soaking for at least 450 s resulted in the formation of shallow microcracks, maximum

10 μm by depth. Even longer annealing times of 600 and 900 s lead to further decrease in crack depth. In addition, the smaller percentage of cracks penetrating the steel (Table 2) suggests that the embrittling effect of zinc is decreasing as the average amount of zinc in the coating is smaller. This result is in line with the findings of Janik et al.[11] who observed that longer soaking time at 900 °C reduced the microcrack depth due to lower zinc concentration in the coating. Moreover, the researchers pointed out that longer annealing time results in the formation of less wavy steel/coating interface leading to smaller number of zinc-rich pockets.
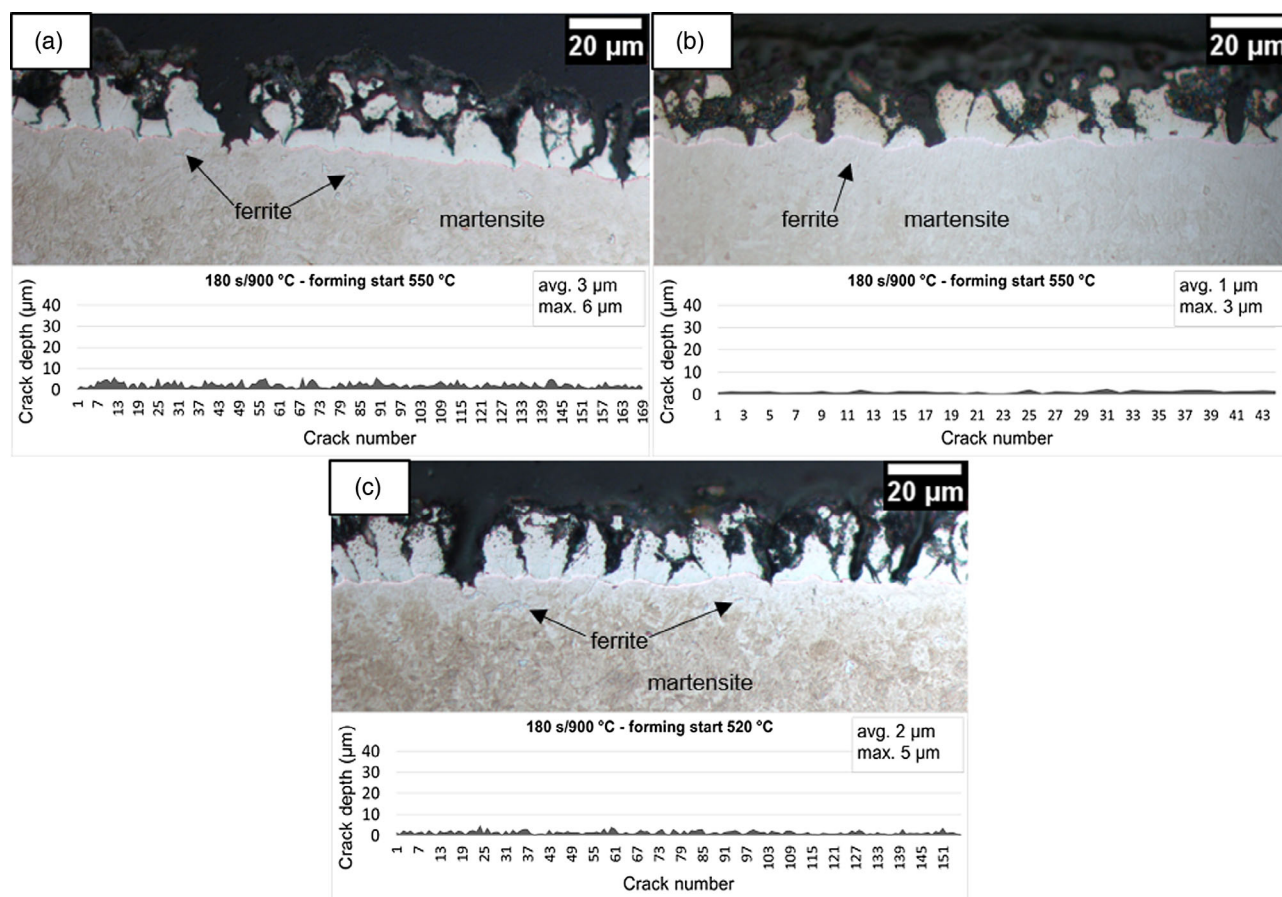
2100112 (11 of 18)

Figure 10. Optical micrographs and crack profiles of the outer wall regions of the DHPF samples of 22MnMoB8 annealed for 180 s at 900 °C. a) 550 °C (dry); b) 550 °C (lubricated); and c) 520 °C (dry). Etching with 2% Nital.

They suggested that these pockets act as an immediate source of zinc to diffuse toward austenite grain boundaries, which facilitates the MIE mechanism. Similar trend in crack depth and soaking time has also been reported by Kim et al.[9] However, they evaluated that the stronger internal oxidation of the coating layer could also decrease the strain concentration and reduce the penetration depth of microcracks.

4.2. Effect of Steel Phase Structure Below Coating/Steel Interface

In the current study, the hot forming temperature was controlled by means of passive air cooling. This type of forming temperature control has effect on several factors contributing to the microcracking. These factors can be listed as follows: the possible onset of ferrite (pearlite) and bainite formation, changes in the flow stress of steel affecting the shear stress of the surface, changes in the friction coefficient between tool and sample, and temperature-dependent diffusion rate of atoms, which in this context can be connected to the possible embrittling effect from zinc or zinc-rich intermetallic phases such as Γ–Fe–Zn.

Considering the steels' susceptibility to microcracking, the microstructure below coating/steel interface should be pointed out. HPF samples of 22MnB5 show typically a small amount of ferrite below coating/steel interface,[7] which is also observed in the current study (Figure 9–12). In conventional HPF temperatures and transfer times, the formation of ferritic phase constituents can be explained with deformation-induced ferrite formation (DIF) mechanism, meaning that the hot deformation of austenite increases the critical cooling rate of steel.[26] The surface region is susceptible to ferrite formation due to high friction forces, which create shear stress to the surface. In addition, the measured elemental profiles (Figure 7) show that the amount of boron is interestingly very low below steel/coating interface, only 5–15 ppm, compared with the reported ladle analysis values of 20–30 ppm (Table 1). As the boron has a crucial role in preventing the nucleation of ferrite,[27] the depletion of boron below coating/steel interface can be connected to increased driving force for ferrite formation. Moreover, a recent study of Arndt et al.[28] suggests that the presence of α-Fe(Zn) in the coating may also facilitate the subsequent formation of zinc-free ferrite. Also, this mechanism may contribute to the typically occurring ferrite formation below coating/steel interface.

Drillet et al.[7] pointed out that in the conditions of their study, a typical microcrack depth observed from the outer wall of HPF components was 10–12 μm. On the contrary, microcracks as deep as 20–50 μm have been met in case of bad contact
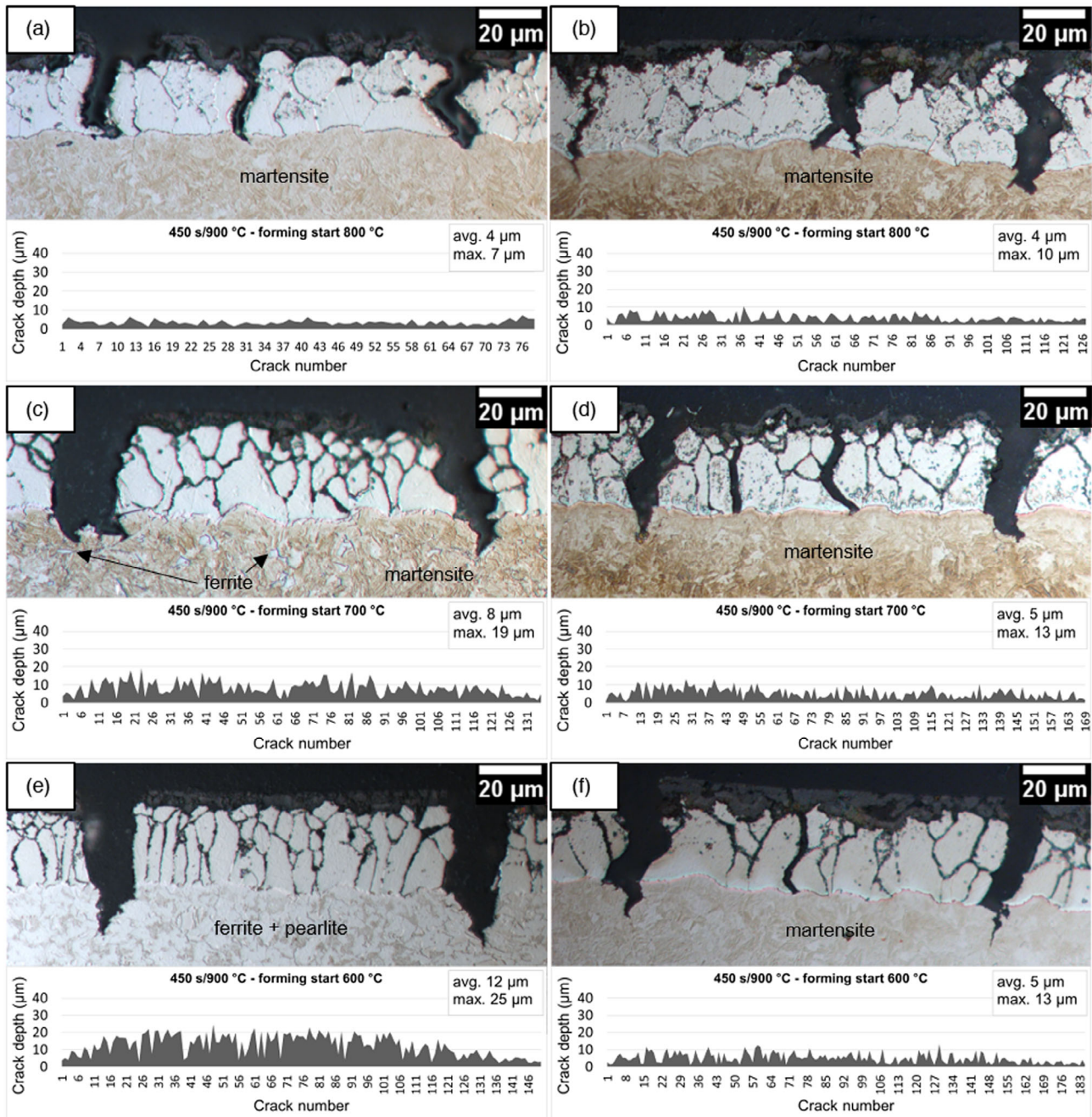
Figure 11. Optical micrographs and crack profiles of the outer wall regions of the HPF samples annealed for 450 s at 900 °C. a) 22MnB5–800 °C; b) 22MnMoB8–800 °C; c) 22MnB5–700 °C; d) 22MnMoB8–700 °C; e) 22MnB5–600 °C; and f) 22MnMoB8–600 °C. Etching with 2% Nital.

conditions. The mentioned crack depths are roughly in line with the results of the current study (Table 2 and 3). Drillet et al.[7] suggested that microcrack depth correlates with the thickness of the heterogeneous subsurface layer consisting of fragmented ferrite and martensite. In turn, Kim et al.[9] noted that the microcrack depth is independent of the substrate microstructure when conventional, i.e., high forming temperatures are applied. To analyze the role of ferrite or heterogeneous subsurface layer more in details, **Figure 14** shows the correlation between ferrite

fraction (in some ultimate cases ferrite + pearlite) and maximum crack depth in HPF samples. The distinction between DIF and conventional forms of ferrite is challenging and would require comprehensive studies with advanced methods of microscopy. Therefore, only the evaluative values of ferrite fractions are presented here to see the trends.

In case of 22MnB5, the longer air-cooling time resulted in the larger amount of ferrite below the coating/steel interface (Table 3). In case of short annealing time of 180 s (Figure 14a),
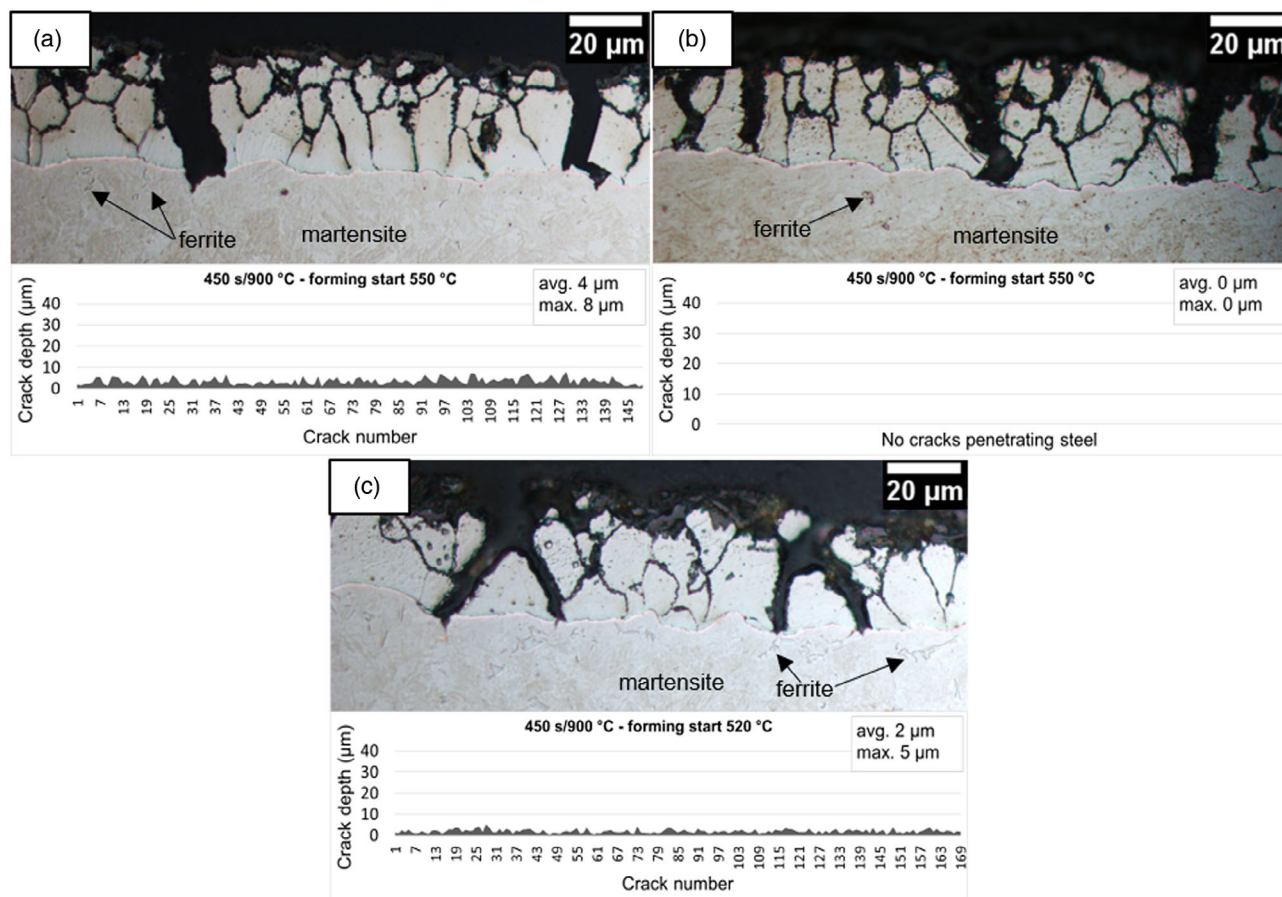
Figure 12. Optical micrographs and crack profiles of the outer wall regions of the DHPF samples of 22MnMoB8 annealed for 450 s at 900 °C. a) 550 °C (dry); b) 550 °C (lubricated); and c) 520 °C (dry). Etching with 2% Nital.
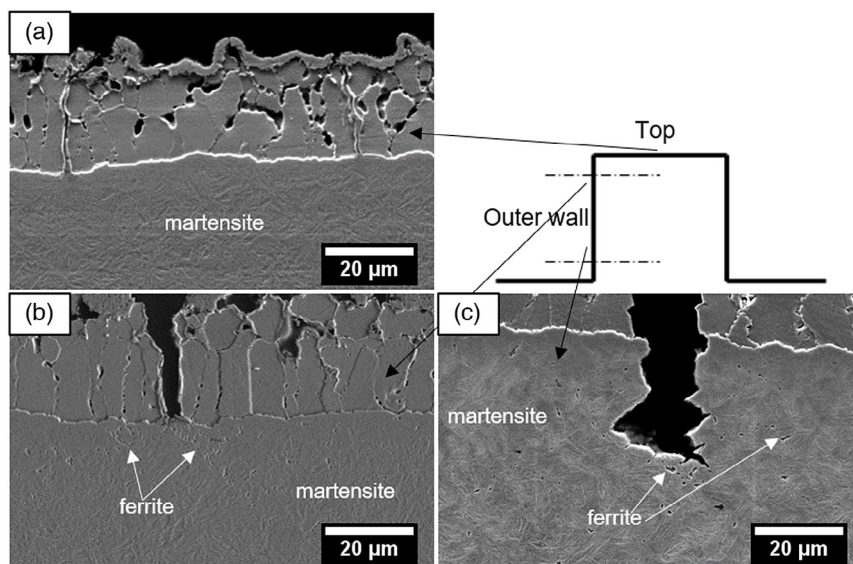

Figure 13. a) A SEM micrograph from top region of the HPF hat profile (no deformation) sample showing 100% martensitic phase structure below coating/steel interface; b) lower region of the HPF sample showing fragmented ferrite in vicinity of tip of a microcrack penetrating the steel. Etching with 2% Nital.
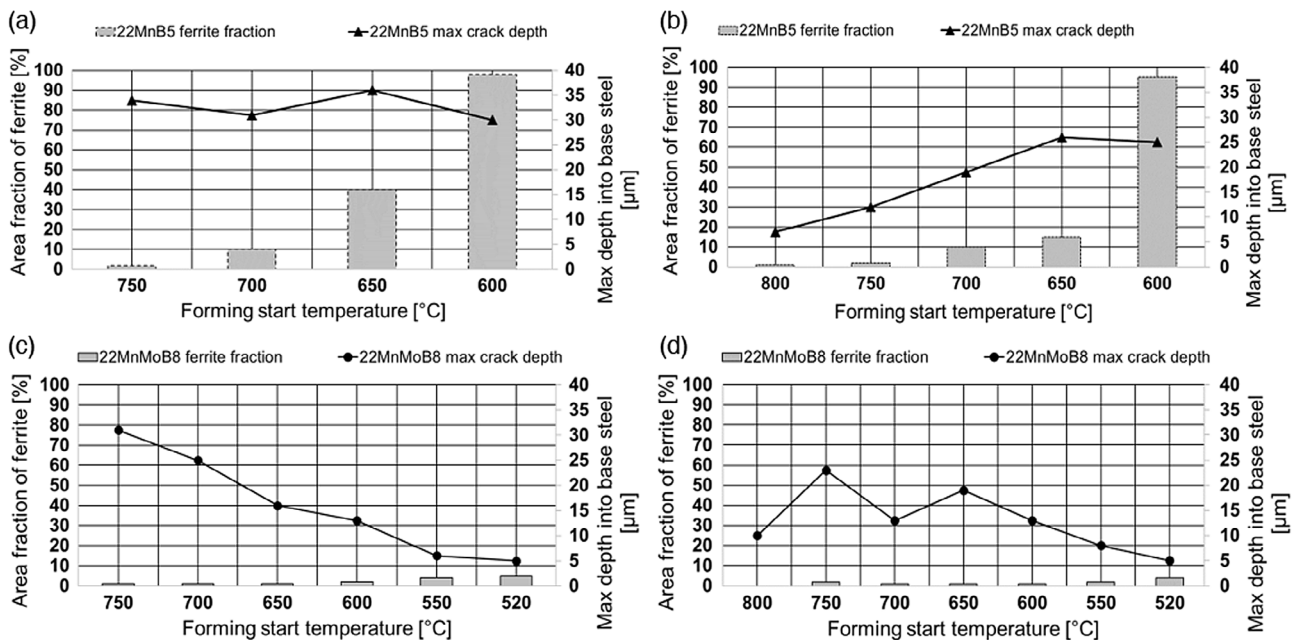
**ADVANCED
SCIENCE NEWS**

www.advancedsciencenews.com

**steel
research**
international

www.steel-research.de

Figure 14. Relationship between sub-surface microstructure (down to 30 μm depth from coating/steel interface) and maximum crack depth as a function of forming start temperature for a) 22MnB5, furnace time 180 s; b) 22MnB5, furnace time 450 s; c) 22MnMoB8, furnace time 180 s; and d) 22MnMoB8, furnace time 450 s.

there is no correlation between ferrite fraction and maximum crack depth of 22MnB5 samples. However, in the case 450 s, the larger amount of ferrite correlates well with the microcrack depth all the way down to forming start temperature of 650 °C after which there is a plateau at 600 °C (Figure 14b). The linear trend of longer annealing time could be explained with the weakening of MIE mechanism as the zinc concentration of the coating is constantly reducing as a function of soaking time. Despite this, the promoting role of subsurface ferrite can be questioned because lower forming temperature is also increasing the flow stress of 22MnB5 steel,[29] which itself could explain the deeper microcracks observed at lower forming temperatures.

However, the overall results of the current study strongly suggest that the presence of ferrite promotes the microcrack penetration. As the first evidence, the outer radius of 22MnB5 samples with higher ferrite contents shows greater tendency to microcracking than 22MnMoB8 after annealing at 180 s (Table 3). The area of outer radius is not subjected to friction forces, and thus the formed microcracks are relatively shallow. Second, the microcrack depth of the outer wall of 22MnMoB8 samples with very small ferrite fractions is generally much smaller compared with the 22MnB5 samples with higher ferrite fractions (Table 3). In addition, as overall the percentage of cracks penetrating the steel is higher in 22MnB5, indicating that the heterogeneous subsurface microstructure consisting of ferrite and austenite is increasing steel susceptibility to more severe microcracking. The only exceptions are the results obtained at high forming temperatures of 800 and 750 °C: for those the amount of ferrite is very limited also in 22MnB5. In the case of 750 °C, 22MnMoB8 shows higher number of cracks penetrating the steel and deeper cracks compared with 22MnB5. It can be

evaluated that the hot strength of 22MnMoB8 is higher due to Mo alloying,[30] resulting in larger flow stress and consequently larger shear stress of the surface. The larger stress level can be assumed to lead to the deeper cracks. In case of high forming temperatures of 800 and 750 °C, the formed ferrite must be mainly DIF by type because the onset of ferrite transformation is far at these temperatures (Figure 1). The contribution of film-like DIF, presence of MIE from zinc, and larger flow stress of 22MnMoB8 could explain deeper microcracks compared with 22MnB5.

To support our conclusion about the promoting role of soft high-temperature ferrite, the detrimental effect of ferrite on the hot ductility of low carbon steels has been widely observed elsewhere. Suzuki et al.[31] reported that the formation of thin film-like proeutectoid ferrite has an embrittling effect on carbon steels when formed on austenite grain boundaries during tensile deformation at high temperatures of 1000–600 °C. The explanation is that the plastic deformation is concentrating on the ferrite until the failure occurs. Similarly, Calvo et al.[32] observed the hot-ductility loss in C–Mn steels at two phase region γ → α in temperatures close to 700 °C due to formation of thin ferritic film on austenite grain boundaries. Dimatteo et al.[33] noted the same effect in a press hardening steel of 35MnB5 type by explaining that ferrite is softer than austenite at elevated temperatures due to higher dynamic recovery rate. This presence of ferrite results in strain concentration peaks in ferritic film, leading to microvoid formation and finally to crack propagation. Coming back to the results of current study, the mutual differences in the measured crack penetration depths between 22MnB5 (higher tendency to ferrite formation) and 22MnMoB8 (low tendency to ferrite formation) are indicating that the formation of high-temperature ferrite leading to heterogeneous subsurface microstructure

should be avoided when aiming for minimizing the steel susceptibility to microcracking during press hardening.

The behavior of 22MnMoB8 (Figure 14c,d) points out a strong correlation between hot forming temperature and microcrack depth. In this case, there is no linear correlation between the amount of subsurface ferrite and microcrack depth. The optical micrographs (Figure 9–12) do not indicate that the cracks would regularly propagate along the paths formed by the small areas of fragmented ferrite, which is considering the high hardenability (Figure 1b) most likely DIF by type. The regions of the crack tips are, however, typically showing the small amounts of fragmented ferrite (Figure 13), which supports the DIF mechanism in vicinity of deformed crack tips. To sum up, the results of 22MnMoB8 are suggesting that the ferrite itself is not the primary embrittling factor in zinc-coated press hardening steels (PHS), but heterogeneous microstructure at the time of hot deformation (ferrite + austenite) makes steel prone to more severe microcrack penetration in locations where tensile stresses and/or high friction forces are simultaneously present.

4.3. Effect of Forming Temperature

As shortly mentioned earlier, the results of 22MnMoB8 show strong correlation between microcrack depth and forming temperature (Figure 14c,d). This is an interesting finding, assuming that the flow stress of steel is increasing as a function of decreasing hot forming temperature as reported, for example, by Kurz et al.[15] In the conversion-delayed 22MnMoB8 steel, the austenite decomposition is greatly hindered compared with 22MnB5, resulting practically in 100% austenitic structure at the time when hot forming is started. The phase fraction of ferrite is only marginally increasing as a function of decreasing hot forming temperature (Figure 14c,d). This behavior is most likely related to the increased stored energy and its promoting effect to DIF formation at lower deformation temperature.[34] Assuming that the steel substrate is virtually austenitic at the time of hot forming, it is possible to uncouple the effect of forming temperature from the potential promoting effect of ferrite and connect the temperature itself with the microcrack depth. The hot forming temperature, in turn, is still connected to two essential factors: flow stress of the steel and diffusion rate of atoms, which control the SME mechanism.[35] As the flow stress of the steel is higher at lower deformation temperatures, the significant decrease in the microcrack depth is emphasizing the strong effect of zinc or zinc-rich phases causing MIE. According to the MIE theories summarized by Lynch,[36] the severity of MIE is decreasing as a function of deformation temperature in relation to the melting temperature of embrittling metal or phase. It is important to mention that the decreasing trend in the microcrack depth of 22MnMoB8 is similar in short and long annealing times (Table 3), indicating that mobility of zinc atoms seems to be a primary and the amount of zinc atoms the secondary factor. This is an essential finding keeping in mind the desired corrosion protection capacity provided by zinc-rich intermetallic ZnFe phases, i.e, Γ-phase, is still present in the coating after the short annealing times as the coating solidifies during intermediate cooling step.[24]

When aiming for minimized penetration depth of cracks, the important role of low hot forming temperature is supported by the results of earlier studies conducted by means of accelerated cooling experiments.[16] The formation of cracks is minimized as the lower forming temperature can eliminate the presence of liquid phases as well as crucially limit the diffusion rate of zinc atoms which have been suggested to play key role in embrittling the steel substrate through SME mechanism proposed by Hensen et al.[16] Characteristic to SME mechanism, the surface self-diffusion of zinc atoms is facilitated by high temperature and can occur along the propagating crack tip. Despite this credible theory, the scientists have struggled for years to find undisputed proof of the embrittling effect of zinc or zinc-rich phases in the absence of liquid phases. Janik et al.[11] observed Zn diffusion into austenite grain boundaries but were not able to connect diffusion depth with the microcrack depth. Later, Hofer et al.[17] were not able to find Zn on the prior austenite grain boundaries of annealed samples. However, a very recent study of Arndt et al.[28] finally found small amounts of zinc in the tips of microcracks and on some of the prior austenite grain boundaries with sophisticated characterization methods, including transmission electron microscopy + focused ion beam (TEM + FIB) and Auger electron spectroscopy (AES). More interestingly, their study suggests that zinc atoms do not diffuse to all prior austenite grain boundaries, which can explain the conflicting results in earlier studies. In any case, the presence of zinc on the surface of microcracks and study shows evidence that MIE is playing a significant role in the penetration of microcracks.

However, the aforementioned conclusions on the undisputed role of MIE do not explain why the crack depth of 22MnB5 samples is the smallest at the highest forming temperature, namely, 800 °C (Table 3). Recalling that the austenite is very soft at 800 °C, the resulting flow and surface shear stresses stay at low level. In addition, the formation of soft ferritic phases is practically eliminated at exceptionally high forming temperature, excluding the possible other promoting factor as well. Therefore, this finding supports the earlier observed characteristics of MIE: the embrittling effect is strongly controlled also by friction and surface stress.

4.4. Role of Stress/Strain and Friction

Choi et al.[37] showed that the microcrack depth of zinc-coated 22MnB5 increases as a function of effective strain. Therefore, larger die radius decreases the microcrack depth as noted earlier by Kim et al.[9]. The researchers found out that larger radius enlarges the contact area which decreases the shear stresses of the surface. In addition to analyzing the penetration depth of cracks, some researchers have focused on the form or appearance of crack tips. The so-called V-shaped microcracks have been connected to the presence of SME mechanism[11] and large friction forces and shear stresses of the surface.[7] Therefore, decreasing the amount of surface shear stress plays a key role in controlling the microcracking.

The beneficial role of lubrication has been reported in earlier studies.[7,10] In the current study, the V-shaped cracks were hardly met at the highest forming start temperatures of 800 °C but were generally the main crack type when formed at lower temperatures. This finding suggests that the high forming temperature results in the desired flow behavior of the steel, whereas

**ADVANCED
SCIENCE NEWS**

www.advancedsciencenews.com

**steel
research**
international

www.steel-research.de

the increasing flow stress at low forming temperatures increases the surface shear stress. Likewise, lubrication decreases the magnitude of surface shear stress, and thus aids in reducing the microcrack penetration depth. However, the shallow cracks in 22MnMoB8, attained at low forming start temperatures of 550 and 520 °C (Figure 10a and 12a), are mainly V-shaped by type. This can be explained with the high flow stress of the steel resulting in high surface shear stress. In the current study, the use of lubrication eliminated the presence of V-shaped cracks (Figure 10b and 12b). Simultaneously, the percentage of cracks penetrating the steel dropped dramatically or was eliminated, indicating that MIE mechanism is not active with the combination of low surface shear stress and low mobility of diffusion zinc atoms.

The role of coating thickness and phase structure on the friction coefficients and magnitude of shear stresses has also received limited attention in the literature. The friction coefficient measurement results reported by Kurz et al.[15] suggest that the friction coefficient of thicker 90/90 g m^{-2} ZnFe coating is smaller compared with 70/70 g m^{-2}. Whereas the researchers do not discuss any details, it can be speculated that differences in the friction coefficient are caused by dissimilar phase structures and oxide layer thicknesses which are inherited from the initial coating thickness and used annealing parameters. However, these effects and further discussion will be left the scope of the current study.

4.5. Beneficial Role of Steel Hardenability

Increased hardenability of steel enables the formation of almost purely martensitic microstructure even after relatively long passive air cooling or transfer times between furnace and HPF. In the current study, the passive air cooling down to temperature of 520 °C was successfully attained for conversion-delayed 22MnMoB8 steel: martensitic microstructure with marginal amount of subsurface ferrite was attained (Figure 10 and 12). In case of 22MnB5, the natural air cooling resulted in the formation of undesired heterogeneous phase structure of the steel, which promoted the formation of deeper microcracks as well as low hardness. Therefore, improved hardenability of steel enables using more arbitrary cooling paths prior to hot forming and finally to increase the robustness of the production by means of limiting the microcrack depth with the simultaneous hardness and strength guarantee.

Kurz et al.[15] found out that accelerated precooling step (cooling rate at least 50 °C s^{-1}) and conversion-delayed steel 20MnB8 help to minimize microcrack depth in ZnFe-coated PHS. The current study implies that also the passive air-cooling step can be successfully applied in direct press hardening process as far as the chemical composition of the steel is optimized. The obtained results suggest that the elimination of ferrite (in practice minor amounts of ferrite may always be formed) will not lead to microcrack-free components if the HPF step is conducted at temperatures above 600 °C. In turn, the role of forming temperature seems to be the most dominant factor in microcracking. At low hot forming temperatures below 600 °C, the flow stress of steel is relatively high, and thus the decreasing trend in microcracking emphasizes the significance of MIE mechanism

facilitated by zinc from the coating. As noted by Lynch,[36] the MIE mechanism is stress and temperature sensitive. Even though it has been shown that the improved hardenability of steel and optimal forming temperature are essential ways to minimize the microcracking, totally crack-free parts can be guaranteed only by optimizing the tribological conditions between tool and steel as well as applying clever geometrical design whenever possible.

5. Conclusions

The crack depth of ZnFe-coated 22MnB5 and 22MnMoB8 was constantly reduced as a function of soaking time at 900 °C when subsequently hot press formed at high temperature of around 800 °C. This behavior, reported earlier also in the literature, can be connected with the decreased amount of zinc in vicinity of coating/steel interface and simultaneous weakening of MIE mechanisms facilitated by the presence of zinc atoms with high mobility.

The maximum microcrack depths, analyzed from the outer radius and outer wall regions of hat-profiled HPF samples, suggest that heterogeneous microstructure consisting of ferrite + austenite (austenite transforms into martensite during quenching) below coating/steel interface increases steel susceptibility to deeper microcrack penetration during HPF.

Whereas the minimization of the ferrite formation can be seen beneficial from the final properties point of view, reduced hot forming temperature plays the most crucial role in decreasing the materials susceptibility to microcracking. The observed behavior is most likely connected to the embrittling effect of zinc or zinc-rich phases via MIE mechanism which has strong temperature dependency.

The microcrack analysis of the current study suggests that the optimal forming temperature is preferably in the range of 500 °C than, for example, around 600 °C. Without further optimization of the hot forming conditions of the 22MnMoB8 steel, depth of all microcracks stayed under 5 μm when forming was started at 520 °C.

Increasing the hardenability of steel, for example, using the studied 22MnMoB8 grade instead of standard 22MnB5 grade, enables the application of exceptionally low hot forming temperatures of around 550–500 °C without special cooling procedures or equipment, and helps to minimize microcrack penetration depth to the promising levels compared with standard 22MnB5 steel.

The results of the current study suggest that totally crack-free parts can be only guaranteed in the conditions where stresses from tribological and mechanical origins are minimized (e.g., by means of lubricated die and optimized component and tool design) and combined with the application of low hot forming temperatures. The importance of surface stress increases from the stress sensitivity of MIE mechanism discussed in the literature.

Lubrication is a reckoned way to decrease shear stress of the surface and through that avoids the formation of sharp V-shaped cracks penetrating the steel. It can be evaluated that decreasing the hot forming temperature below 550 °C can also open new possibilities for applying lubrication in serial production of HPF components.

Conflict of Interest

The authors declare no conflict of interest.

Data Availability Statement

Research data are not shared.

[1] P. Åkerström, M. Oldenburg, *J. Mater. Process. Technol.* **2006**, *174*, 399.

[2] H. Karbasian, A. E. Tekkaya, *J. Mater. Process. Technol.* **2010**, *210*, 2103.

[3] D. Fan, H. Kim, B. De Cooman, *Steel Res. Int.* **2009**, *80*, 241.

[4] D. Fan, B. De Cooman, *Steel Res. Int.* **2012**, *83*, 412.

[5] A. R. Marder, *Prog. Mater. Sci.* **2000**, *45*, 191.

[6] J. Singh, J. Hall, J. Jason, in *Proc. of the 4th Int. Conf. on Hot Sheet Metal Forming of High-Performance Steel* (Eds: M. Oldenburg, K. Steinhoff, K. B. Prakash), Verlag Wissenschaftliche Scripten, Auerbach, Germany, Luleå **2013**.

[7] P. Drillet, R. Grigorieva, G. Leuillier, T. Vietoris, *La Metall. Ital.* **2012**, *1*, 3.

[8] G. Hensen, W. Melfo, S. Chen, R. Bleeker, W. Verloop, in *Proc. of the 4th Int. Conf. on Hot Sheet Metal Forming of High-Performance Steel* (Eds: M. Oldenburg, K. Steinhoff, K. B. Prakash), Verlag Wissenschaftliche Scripten, Auerbach, Germany, Luleå **2013**, pp. 463–470.

[9] S. Kim, I. Son, D. Kim, S. J. Kim, in *Proc. of the 4th Int. Conf. on Hot Sheet Metal Forming of High-Performance Steel* (Eds: M. Oldenburg, K. Steinhoff, K. B. Prakash), Verlag Wissenschaftliche Scripten, Auerbach, Germany, Luleå **2013**, pp. 537–544.

[10] M. Köyer, J. Banik, S. Graff, J. F. Lenze, G. Parma, S. Sikora, in *Proc. of the 4th Int. Conf. on Hot Sheet Metal Forming of High-Performance Steel* (Eds: M. Oldenburg, K. Steinhoff, K. B. Prakash), Verlag Wissenschaftliche Scripten, Auerbach, Germany, Luleå **2013**, pp. 363–370.

[11] V. Janik, Y. Lan, P. Beentjes, D. Norman, G. Hensen, S. Sridhar, *Metall. Mater. Trans. A* **2016**, *47*, 400.

[12] J. Kang, D. Kim, D. H. Kim, S. Kim, *Surf. Coat. Technol.* **2019**, *357*, 1069.

[13] P. J. Belanger, R. Labrie, A. Pearson, G. Telleck, in *Proc. of the 4th Int. Conf. on Hot Sheet Metal Forming of High-Performance Steel* (Eds:

M. Oldenburg, K. Steinhoff, K. B. Prakash), Verlag Wissenschaftliche Scripten, Auerbach, Germany, Luleå **2013**, pp. 119–126.

[14] T. Kurz, H. Schwinghammer, G. Luckeneder, T. Manzenreiter, A. Sommer, in *Proc. of the 5th Int. Conf. on Hot Sheet Metal Forming of High-Performance Steel* (Eds: M. Oldenburg, K. Steinhoff, K. B. Prakash), Verlag Wissenschaftliche Scripten, Auerbach, Germany, Toronto **2015**, pp. 345–353.

[15] T. Kurz, P. Larour, J. Lackner, T. Steck, G. Jesner, I. O. P. Conf. *Ser.: Mater. Sci. Eng. 159* 011001.

[16] G. Hensen, P. Beentjes, M. Abspoel, J. Loiseaux, in *Proc. of the 5th Int. Conf. on Hot Sheet Metal Forming of High-Performance Steel* (Eds: M. Oldenburg, K. Steinhoff, K. B. Prakash), Verlag Wissenschaftliche Scripten, Auerbach, Germany, Toronto **2015**, pp. 85–92.

[17] C. Hofer, T. Kurz, H. Clemens, R. Schnitzer, in *Proc. of the 6th Int. Conf. on Hot Sheet Metal Forming of High-Performance Steel* (Eds: M. Oldenburg, K. Steinhoff, K. B. Prakash), Verlag Wissenschaftliche Scripten, Auerbach, Germany, Atlanta **2017**, pp. 383–390.

[18] N. Saunders, U. K. Z. Guo, X. Li, A. P. Miodownik, J.-P. Schille, *JOM* **2003**, *55*, 60.

[19] H. Järvinen, M. Isakov, T. Nyyssönen, M. Järvenpää, P. Peura, *Mater. Sci. Eng. A* **2016**, *676*, 109.

[20] M. Abbasi, A. Saeed-Akbari, M. Naderi, *Mater. Sci. Eng. A* **2012**, *538*, 356.

[21] K. Nakagawa, T. Nakagaito, T. Yokota, K. Seto, A. Yoshitake, in *Proc. of the 5th Int. Conf. on Hot Sheet Metal Forming of High-Performance Steel*, (Eds: M. Oldenburg, K. Steinhoff, K. B. Prakash), Verlag Wissenschaftliche Scripten, Auerbach, Germany, Toronto **2015**, pp. 77–84.

[22] V. Janik, P. Beentjes, D. Norman, G. Hensen, S. Seetharaman, in *Proc. of the Materials Science and Technology (MS&T) 2014*, Pittsburg, October **2014**.

[23] L. Cho, H. Kang, C. Lee, B. C. De Cooman, *Scr. Mater.* **2014**, *90–91*, 25.

[24] C. Dever, J. McDermid, Y. Kim, J. Kish, F. Goodwin, in *Proc. of the EUROCORR 2017*, Prague, September **2017**.

[25] H. Järvinen, M. Honkanen, M. Patnamsetty, S. Järn, E. Heinonen, H. Jiang, P. Peura, *Surf. Coat. Technol.*, **2018**, *352*, 378.

[26] M. Somani, L. P. Karjalainen, M. Eriksson, M. Oldenburg, *ISIJ Int.* **2001**, *41*, 361.

[27] A. Terzic, M. Calcagnotto, S. Guk, T. Schulz, R. Kawalla, *Mat. Sci. Eng. A* **2013**, *584*, 32.

[28] M. Arndt, T. Truglas, J. Duchoslav, K. Hingerl, D. Stifter, C. Commenda, J. Haslmayr, S. Kolnberger, J. Faderl, H. Groiss, arXiv e-prints, arXiv:2007.01136, v1, submitted.

[29] M. Merklein, J. Lechler, *J. Mater. Process. Technol.* **2006**, *177*, 452.

[30] C. Martins de Abreu, E. Poliak, L. B. Godefroid, N. Fonstein, *ISIJ Int.* **2014**, *54*, 227.

[31] H. G. Suzuki, S. Nishimura, J. Imamura, Y. Nakamura, *Trans. ISIJ* **1984**, *24*, 169.

[32] J. Calvo, A. Rezaeian, J. Cabrera, S. Yue, *Eng. Fail. Anal.* **2007**, *14*, 374.

[33] A. Dimatteo, G. Lovicu, M. DeSanctis, R. Valentini, in *Proc. of the 4th Int. Conf. on CRACK PATHS (CP 2012)*, Gaeta, September 2012.

[34] W. Yu-Qing, S. Xin-Jun, D. Han, *Iron Steel* **2005**, *40*, 9.

[35] M. H. Kamdar, in *Proc. of the 6th Int. Conf. on Fracture*, (Eds: S.R. Valluri, D.M.R. Taplin, P.R. Rao, J.F. Knott, R. Dubey), New Delhi **1984**, pp. 3837–3849.

[36] S. P. Lynch, *J. Fail. Anal. Prev.* **2008**, *8*, 259.

[37] J. W. Choi, K. S. Oh, H. G. Kim, D. J. Kim, *ISIJ Int.* **2019**, *59*, 1295.